

Melanin concentration maps by label-free super-resolution photo-thermal imaging on melanoma biopsies

MARGAUX BOUZIN,^{1,5} MARIO MARINI,^{1,5} GIUSEPPE CHIRICO,^{1,2,6} FRANCESCA GRANUCCI,³ FRANCESCA MINGOZZI,³ ROBERTO COLOMBO,⁴ LAURA D'ALFONSO,¹ LAURA SIRONI,¹ AND MADDALENA COLLINI^{1,2,7}

¹Physics Department, Università degli Studi di Milano-Bicocca, Piazza della Scienza 3, 20126, Milano, Italy

²CNR Institute for Applied Science and Intelligent Systems, Via Campi Flegrei 34, 80078, Pozzuoli, Italy

³Biotechnology and Biosciences Department, Università degli Studi di Milano-Bicocca, Piazza della Scienza 2, 20126, Milano, Italy

⁴Department of Earth and Environmental Sciences, Università degli Studi di Milano-Bicocca, Piazza della Scienza 1, 20126, Milano, Italy

⁵Equal contribution

⁶giuseppe.chirico@unimib.it

⁷maddalena.collini@unimib.it

Abstract: Surgical excision followed by histopathological examination is the gold standard for melanoma screening. However, the color-based inspection of hematoxylin-and-eosin-stained biopsies does not provide a space-resolved quantification of the melanin content in melanocytic lesions. We propose a non-destructive photo-thermal imaging method capable of characterizing the microscopic distribution and absolute concentration of melanin pigments in excised melanoma biopsies. By exploiting the photo-thermal effect primed by melanin absorption of visible laser light we obtain label-free super-resolution far-infrared thermal images of tissue sections where melanin is spatially mapped at sub-diffraction 40- μm resolution. Based on the finite-element simulation of the full 3D heat transfer model, we are able to convert temperature maps into quantitative images of the melanin molar concentration on B16 murine melanoma biopsies, with $4 \cdot 10^{-4}$ M concentration sensitivity. Being readily applicable to human melanoma biopsies in combination with hematoxylin-and-eosin staining, the proposed approach could complement traditional histopathology in the characterization of pigmented lesions ex-vivo.

© 2022 Optica Publishing Group under the terms of the [Optica Open Access Publishing Agreement](#)

1. Introduction

Melanomas are malignant tumors originating from pigment-producing melanocytes in the skin [1–4]. Worldwide annual incidence rates have increased by nearly 50% over the past decade (with ~325000 diagnoses of melanoma skin cancer reported worldwide in 2020 [5]), and the extremely aggressive nature of melanomas in metastasizing to distant organs is often associated to unfavorable prognosis [6]. The resulting high mortality, cost and complexity of care pose significant social burdens and demand for the elucidation of the still unclear biological mechanisms underlying melanomas [4] and for the development of effective early-stage diagnostic tools, which are essential to successful treatment [7]. In this context, novel quantitative methods are required to complement and strengthen the robustness of standard histopathological analyses, which still currently rely on a partially subjective visual inspection of immunohistochemistry-stained or hematoxylin-and-eosin (h&e) stained biopsies [8–11].

A major function differentiating normal and malignant melanocytes involves the synthesis of melanin [12]. Although the detailed structure of the final products of melanin biosynthesis is still unknown [13,14], it is widely recognized that melanogenesis is controlled by nutritional, hormonal and physicochemical factors [15], and that it consists in a multistep transformation of L-tyrosine and L-DOPA (L-3,4-dihydroxyphenylalanine) into melanin biopolymers via oxidoreduction reactions [15–17]. Melanogenesis can be highly deregulated in melanomas [2,15] and may favor tumor progression due to immunosuppressive, genotoxic and mutagenic properties [12,15]. The production of pigment has been pointed out as adversely affecting the clinical outcome of metastatic melanomas [15], it attenuates the tumor susceptibility to radio- and chemo-therapy [16] and plays a controversial role in regulating melanoma invasiveness [2,16]. Melanin provides the necessary protection against ultraviolet radiation and reactive oxygen species in the skin [15], and, at the same time, acts as a marker for melanocyte differentiation [15] serving as potential diagnostic tool [16]. Overall melanin behaves as a double-edge sword [12,16] in providing an antioxidant and photoprotective shield while playing a regulatory role in cancer evolution [18]. Such a role has suggested the exploitation of the melanin concentration and spatial distribution as informative biomarkers, to be included in synoptic reports by pathologists, to complement the aforementioned standard histopathological analyses of pigmented skin lesions [9,12].

Analytical techniques aimed at quantifying melanin in biological samples often rely on destructive chemical degradation and analysis [9], and perform in-vitro assays on 2D and 3D cell cultures by absorption spectroscopy [18], fluorescence spectrophotometry [19] or high performance liquid chromatography [20] with no spatial resolution [21]. Similarly, Raman spectroscopy [22] and electron paramagnetic resonance spectrometry [23] are less invasive, but still limited to single-point or low-resolution (~ 0.5 mm) experiments, thereby being insensitive to the spatial distribution of melanin in the putative melanoma.

To our knowledge, non-destructive and label-free high resolution melanin-based imaging ex-vivo has only been demonstrated on human and murine melanoma and on human retinal pigment epithelium by sophisticated optical methods, ranging from fluorescence lifetime (FLIM) imaging [24] and confocal reflectance microscopy [25,26] to pump-and-probe spectroscopy [9,27], Photo-Acoustic Microscopy (PAM) [28] and Photothermal Imaging (PHI) [29–32]. Both the dominant melanin species (eumelanin and pheomelanin) exhibit a peculiar monotonically decreasing absorption spectrum in the 300–1100 nm range [14,22], and give rise to fluorescence emission upon near-infrared two-photon excitation [33,34] or to a highly efficient thermal relaxation upon visible to near infrared light absorption. Despite the moderate melanin fluorescence quantum yield [14], FLIM imaging has allowed differentiating histologically-confirmed benign and malign melanocytic skin lesions by keratinocytes-melanocytes classification [24]. On the other hand, PHI [29–31], PAM [28] and pump-probe imaging [9,27] map the spatial distribution of eu- and pheo-melanin pigments ex-vivo by taking advantage of non-fluorescent contrast (non-linear refractive index changes, photo-acoustic waves generated by thermo-elastic expansion and transient absorption, respectively), with the main advantages of optical sectioning capability, high sensitivity and sub-micrometer spatial resolution. Major drawbacks of these approaches consist in a limited size (typically less than $100 \times 100 \mu\text{m}^2$) of the imaged fields of view and/or in the exploitation of costly and complex pump-probe experimental setups with lock-in detection schemes. Quantification of the melanin absolute concentration has been only achieved by photo-acoustic microscopy on ex-vivo tissues, where the melanin concentration has been recovered upon calibration on reference phantoms with known melanin content [28].

In this work, we propose an alternative approach aimed at the characterization of the spatial distribution and absolute concentration of melanin pigments in melanoma biopsies by means of super-resolution photo-activated thermal imaging [35,36]. We take advantage of the highly efficient photo-thermal effect primed by melanin absorption of focused low-power (~ 30 mW) visible laser light. We detect the resulting laser-induced local temperature variations in the

sample by far-infrared thermography [37], and exploit our recently-developed super-resolution image acquisition approach [35,36] to spatially map melanin pigments at sub-diffraction tunable $\sim 40\text{ }\mu\text{m}$ resolution over extended ($\text{mm}^2\text{-cm}^2$ sized) tissue sections in label-free configuration. Super-resolved thermal images are subsequently converted into quantitative maps of the melanin absolute molar concentration based on the results of finite-element simulations and the numerical integration of the 3D heat equation in the presence of modulated laser illumination. A concentration lower limit of detection equal to $4\cdot 10^{-4}\text{ M}$ (0.07 mg mL^{-1}) is achieved as a consequence of the employed 33-mW excitation laser power and of the 0.1-K temperature sensitivity of our commercially available thermal camera.

The feasibility of the approach is demonstrated on B16 [6] murine melanoma biopsies. On these samples we are further able for the first time to bring into evidence a multi-peaked distribution of the amplitudes of laser-induced temperature increments and, by the multimodal combination of infrared thermography and fluorescence confocal microscopy, we highlight a negative correlation between the thermal signal amplitude and the size of fluorescently stained cell nuclei. Provided the nuclear size and the melanin content may be related to cellular proliferation [38,39] and maturation stage [9], our results pave the way for the future exploitation of super-resolved infrared thermal imaging for the discrimination of different cellular subtypes in excised pigmented skin lesions.

2. Results and discussion

2.1. Spatial distribution of melanin pigments mapped by super-resolution thermal imaging on B16 murine melanoma biopsies

Conventional non-contact far-infrared thermal imaging provides temperature spatial maps based on the intensity of the thermal $\sim 7\text{-}13\text{ }\mu\text{m}$ radiation emitted by the sample [37]. The radiance R is quantified by a microbolometer-based thermal camera and converted into the sample absolute temperature T under the assumption of grey-body emission according to Stefan-Boltzmann's law ($R = \varepsilon\sigma T^4$, where ε is the grey-body emissivity and $\sigma = 5.67\cdot 10^{-8}\text{ W}/(\text{m}^2\text{K}^4)$ is Stefan-Boltzmann's constant) [37]. The spatial resolution of infrared thermography is theoretically limited at $\sim 0.1\text{-}0.5\text{ mm}$ by diffraction at the low (typically ≤ 0.05) numerical aperture of the collecting Germanium lens. However, the nominal limit is further worsened to an effective value of $\sim 1\text{ mm}$ by both the extended camera pixel size on the sample plane and the thermal wave diffusion in the sample [35], so that a high-resolution thermal characterization of biological samples on the tissue scale by far-infrared conventional thermography is typically prevented.

The resolution enhancement required to image and map melanin pigments in melanoma biopsies ex-vivo is achieved here by the implementation of super-resolution image acquisition. Super-resolved photo-thermal imaging, which has been recently developed by our group [35], relies on a modulated laser illumination of the sample and on the automated localization of the resulting laser-induced temperature variations imaged by a far-infrared thermal camera. Specifically, a programmable shutter is synchronized with the raster scan of a focused low-power visible-wavelength laser beam to prime a sequence of isolated absorption and heat-release events in the sample. Any time the photo-thermal effect takes place, the a-posteriori Gaussian surface fit of the laser-primed temperature peak appearing in the thermal-camera frames allows localizing the corresponding absorptive center with an accuracy that is only limited by the shot noise of thermal emission (i.e., by the images signal-to-noise ratio) and the excitation laser spot size [35]. The illumination and localization procedure is repeated across the entire sample region of interest, and the final super-resolution image is reconstructed and color-coded by the localized centers and amplitudes of all the measured temperature peaks. Provided the excitation laser spot size can be tuned at will down to a diffraction-limited $\sim \mu\text{m}$ size, the spatial resolution is ultimately determined by the $\sim 10\text{-}50\text{-}\mu\text{m}$ peak localization uncertainty achieved with typical detected temperature increments of few degrees [35].

Super-resolution photo-thermal imaging is adopted here to image and quantify melanin pigments at sub-diffraction 40- μm resolution over $\text{mm}^2\text{-cm}^2$ sized excised murine melanoma biopsies. We analyze biopsies of a B16 murine melanoma model excised 14 days upon cells inoculation (*methods* section). The presence of melanin, which is responsible for evident pigmentation of the excised tissue sections, is confirmed by Fluorescence Lifetime Imaging (FLIM). Excitation at 800 nm and detection of the two-photon excited endogenous fluorescence in the 600/40 nm band allows quantifying a double-component fluorescence lifetime, equal to $\tau_1 = (0.51 \pm 0.05)$ ns and $\tau_2 = (2.21 \pm 0.05)$ ns with 21% and 79% relative fractions, respectively. Recovered lifetime values agree with those reported in the literature [24] for melanin-containing melanocytes and keratinocytes and confirm the abundance of melanin pigments in the tissue.

For photo-thermal imaging experiments, we prime light-absorption and photo-thermal effect at the 514-nm wavelength of an Argon beam. With a typical excitation laser power on the sample plane $P_0 = 33$ mW, and a laser activation time $\tau_{\text{on}} = 200$ ms per excitation event, we retrieve temperature increments in the $\overline{\Delta T}_{\text{max}} = 0\text{-}10$ K range (Fig. 1(a)). With these temperature values no photo-damage is induced on the sample, as verified by sequential transmitted-light imaging before and after photo-thermal data acquisitions (Fig. S1). Further confirmation is provided by the possibility of performing hematoxylin-and-eosin staining of the very same tissue section right after the completion of photo-thermal data acquisition (Fig. 1(b)).

As revealed in Fig. 1(a) with the super-resolution photo-thermal image of a typical tissue section, the spatial distribution and the amplitude of laser-induced temperature increments are highly heterogeneous, with only portions of the imaged biopsy effectively contributing to a non-zero detected thermal signal. Visual comparison of the super-resolved thermal map (Fig. 1(a)) with the corresponding conventional transmitted-light image (Fig. S2) and with the image acquired upon hematoxylin-and-eosin staining of the same biopsy (Fig. 1(b)) confirms accurate reconstruction of the sample morphology.

Hematoxylin-and-eosin staining results in cellular nuclei being stained blue and the cells cytoplasm and the extracellular matrix being stained pink [8]; melanin, which is not specifically stained, appears in h&e-stained B16 melanoma as optically contrasted brown-black eumelanosome-like granules [8,16,20]. A close-up inspection of magnified regions of interest in the h&e image (Fig. 1(c),(d)) highlights that melanin is prominently present in those regions of the biopsy where a pronounced photo-thermal effect is detected (Fig. 1(a),(c)), whereas clearly less abundant melanin pigments are observed in those areas where no heat release above the 0.1-K thermal camera sensitivity takes place upon laser irradiation (Fig. 1(a),(d)). Therefore, while not enabling a straightforward routine quantification of the melanin content, the hematoxylin-and-eosin image of the biopsy confirms that the detected thermal signal can be ascribed to the photo-thermal activity of melanin. Such a conclusion is reinforced by the nearly absent photo-thermal signal exceeding the thermal camera sensitivity in less pigmented B16 melanoma biopsies excised 7 days after cells injection (Fig. S3).

The histogram of the amplitudes of laser-induced temperature increments extracted from Fig. 1(a) reveals a multi-peaked distribution (Fig. 1(e)). 20% of the imaged area appears associated to $\overline{\Delta T}_{\text{max}}$ values lying above the 0.1-K thermal camera sensitivity. Above 0.1 K, temperature increments identify two clearly separated peaks, with the lower- and higher-amplitude peaks centered at $\overline{\Delta T}_{\text{max}} = (0.30 \pm 0.08)$ K and $\overline{\Delta T}_{\text{max}} = (1.7 \pm 1.1)$ K, respectively (mean \pm standard deviation). Super-resolved thermal imaging on a selected region of interest of the same biopsy at increased laser activation time $\tau_{\text{on}} = 600$ ms retrieves systematically higher temperature increments, as expected, but still preserves the double-peaked distribution of the detected thermal signal above the camera sensitivity (Fig. 1(e) and Fig. S4). We can therefore exclude that the 0.3-K temperature peak is a spurious result of erroneous Gaussian surface fits performed on the thermal-camera frames at moderately low signal-to-noise ratio. The reproducibility of the results is also highlighted by the superposition of the histograms of laser-induced temperature

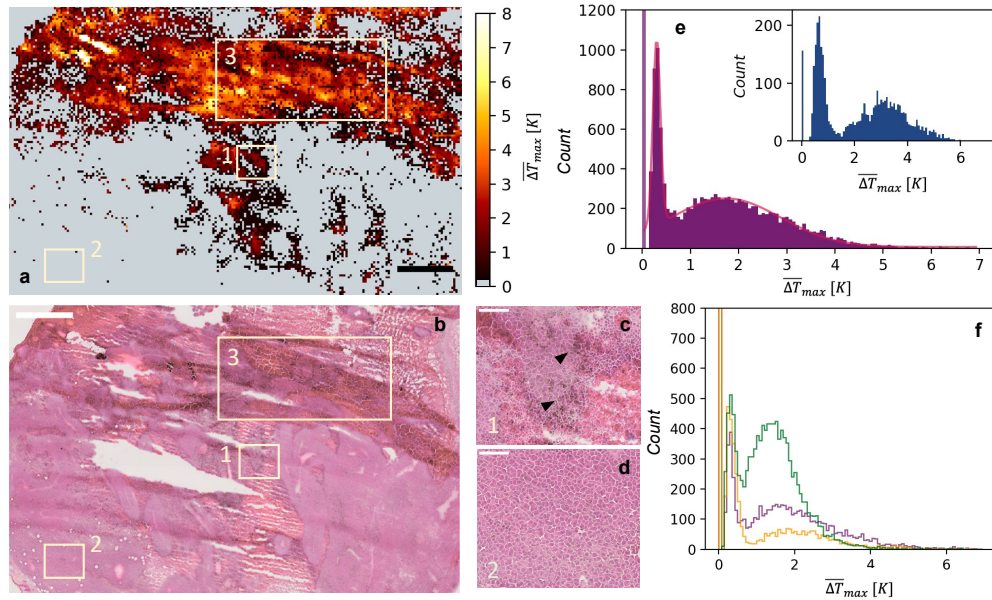


Fig. 1. Sub-diffraction photo-thermal imaging on B16 melanoma biopsies. (a) Super-resolution label-free photo-thermal image of a B16 murine melanoma biopsy. Acquisition parameters: $\lambda_{exc} = 514$ nm, $P_0 = 33$ mW, $\tau_{on} = 200$ ms, laser $1/e^2$ radius $\omega = (28 \pm 1)$ μm , pixel size $\delta x = 37.8$ μm . Notice that grey color codes for pixels where no thermal signal above the thermal camera sensitivity (0.1 K) has been detected. (b) H&E image of the same biopsy imaged in (a). H&E staining has been performed upon completion of photo-thermal imaging. (c,d) Magnification of ROIs 1 and 2 from the h&e image in (b). Black arrows in (c) point to melanin pigments appearing brownish in color. Scale bar = 1000 μm in (a,b), 100 μm in (c,d). (e) Histogram of the amplitude of laser-primed temperature increments detected in (a), overlaid to the best fit to a two-component Gaussian distribution. Best-fit peaks correspond to $\Delta\bar{T}_{max} = (0.30 \pm 0.08)$ K and $\Delta\bar{T}_{max} = (1.7 \pm 1.1)$ K. The y-axis has been limited to the 0-1200 count range for the sake of display. Inset: histogram of the amplitude of laser-primed temperature increments detected in ROI 3 of panel (a) at increased $\tau_{on} = 600$ ms (the corresponding super-resolved thermal image is reported in Fig. S4). (f) Reproducibility of the histogram of the amplitude of laser-primed temperature increments detected in 3 biopsies excised from 3 different tumors under the same imaging conditions of panel (a). Histograms have been derived from equal-sized ROIs (5.2×4.1 mm²).

increments recovered on tissue sections excised from different tumors and imaged under identical conditions (Fig. 1(f)). The multi-peaked signal distribution is preserved, with similar center values and variable relative fractions for the three temperature peaks.

Based on the results of Fig. 1, in the following (i) we demonstrate the conversion of temperature-based images into quantitative maps of the absolute concentration of melanin pigments, and (ii) we combine infrared thermography and fluorescence confocal microscopy in a multimodal approach that allows to elucidate the presence of different cellular populations in the tissue as suggested by the thermal-signal distributions of Fig. 1(e)-(f).

2.2. Super-resolution images of the absolute molar concentration of melanin pigments

The amplitude $\Delta\bar{T}_{max}$ of the temperature increment resulting from a laser-induced photo-thermal effect and sensed by the pixelated detector (focal plane array) of a far-infrared thermal camera is the result of the convolution of the camera point-spread-function with the spatial temperature

profile, followed by the spatial average of the convoluted temperature distribution over the extended camera pixel size. Based on the quartic temperature dependence on the radiance in Stefan-Boltzmann's law, $\overline{\Delta T}_{max}$ at time-point $t = \tau_{on}$ can be therefore expressed as

$$\overline{\Delta T}_{max} = \left\{ \frac{1}{d^2} \iint_{-d/2}^{d/2} N \cdot [T^4(x, y, 0, \tau_{on}) * PSF(x, y)] dx dy \right\}^{1/4} - T_m \quad (1)$$

In this notation T_m , is the room (ambient) temperature, d is the camera pixel-size on the sample plane and

$$N = \frac{\iint_{-\infty}^{+\infty} T^4(x, y, 0, \tau_{on}) dx dy}{\iint_{-\infty}^{+\infty} [T^4(x, y, 0, \tau_{on}) * PSF(x, y)] dx dy} \quad (1b)$$

is the convolution normalization factor. $PSF(x, y)$ is the approximately Gaussian camera point-spread-function on the sample plane, with unit amplitude and diffraction-limited full width at half height ζ assigned by Abbe's law. For the numerical aperture of the thermal camera employed in the present work, $\zeta = 0.61\lambda/N.A. = 265 \mu\text{m}$ at the average 10- μm wavelength of the collected infrared radiation. $T(x, y, 0, \tau_{on})$ represents the temperature spatial distribution on the sample front surface ($z = 0$) at time-point $t = \tau_{on}$, primed by an excitation laser beam centered at $(x, y, z) = (0, 0, 0)$.

We are interested here in the expression for $T(x, y, 0, \tau_{on})$ and $\overline{\Delta T}_{max}$ in the presence of a focused Gaussian laser beam (having power P_0 and $1/e^2$ beam waist ω on the sample plane) impinging on a two-layer material composed of a 1-mm thick glass slide and a 20- μm thick tissue section. The 20- μm layer determines the magnitude of surface light absorption with absorbance A (no light absorption and heat release are observed for a single-layer 1-mm thick glass slide at the adopted incident laser power), whereas the contribution of the 1-mm layer dominates the system thermal response: as verified by finite-element numerical simulations (Fig. S5), the spatial confinement of the deposited power in the upper thin tissue layer allows effectively approximating the sample as a single-layer substrate with absorbance A and thickness $L = 1020 \mu\text{m}$, with the thermal conductivity k and the thermal diffusivity D of the glass layer, and subject to an effective laser power $P_{eff} > P_0$ (Fig. S5). The increased effective laser power allows taking the thermal conductivity of the thin tissue layer (which is lower than the thermal conductivity of the underlying thick glass substrate) into account (Fig. S5). Provided the negligible contribution of both convective and radiative losses (Fig. S6), the laser-primed temperature distribution $T(x, y, z, t)$ on such a thermally thick specimen can be expressed as [36,40]

$$T(x, y, z, t) \approx T_m + P_{eff}(1 - e^{-2.303EC\ell})\phi \frac{2D}{\pi k} \int_{t_0}^t \frac{1}{\omega^2 + 8Dt_1} \exp\left(-\frac{2(x^2 + y^2)}{\omega^2 + 8Dt_1}\right) \frac{1}{\sqrt{\pi Dt_1}} \exp\left(-\frac{z^2}{4Dt_1}\right) dt_1 \quad (2)$$

By definition of absorbance, the absorbed laser power has been expressed in Eq. (2) as $P_{eff}(1 - e^{-2.303EC\ell})$, where $\ell = 20 \mu\text{m}$, E is the molar extinction coefficient of light-absorbing and heat-releasing entities, and C is their molar concentration within the laser-illuminated voxel defined by the thickness ℓ and the excitation laser beam waist. P_{eff} equals $P_{eff} = 1.2P_0$ as quantified in Fig. S5, and the contribution of laser-light reflection by the pigmented tissue is assumed negligible in comparison with absorption [41]. ϕ corresponds to the heat-release efficiency of the photo-thermal sample. In the integral, $t_0 = 0$ if $t < \tau_{on}$ and $t_0 = t - \tau_{on}$ if $t \geq \tau_{on}$. By substituting $T(x, y, 0, \tau_{on})$ from Eq. (2) into Eq. (1) and by numerical integration, the theoretical dependence of $\overline{\Delta T}_{max}$ on the concentration C can be evaluated.

Results are reported in Fig. 2(a) for melanin pigments under the typical experimental conditions adopted here for super-resolution thermography. In the 0-10 K range of our experimentally

measured temperature increments, a linear relation well approximates the dependence of $\overline{\Delta T}_{max}$ on the concentration C . This allows establishing a direct proportionality of the type $\overline{\Delta T}_{max} = mC$ between the experimental amplitudes $\overline{\Delta T}_{max}$ and the concentration of photo-thermal laser-excited pigments in the tissue. In the present case ($d = 420 \mu\text{m}$, $P_{\text{eff}} = 39.6 \text{ mW}$, $\tau_{\text{on}} = 200 \text{ ms}$, $\omega = 30 \mu\text{m}$, $\ell = 20 \mu\text{m}$, $k = 0.9 \text{ Wm}^{-1}\text{K}^{-1}$, $D = 5.02 \cdot 10^{-7} \text{ m}^2\text{s}^{-1}$, $\phi = 0.99$ [42] and $\varepsilon = 1500 \text{ M}^{-1}\text{cm}^{-1}$ for melanin at the 514-nm excitation wavelength [43]), the slope m equals $m = 254 \text{ KM}^{-1}$. Super-resolution photo-thermal images of melanoma biopsies can be therefore converted into quantitative maps of the absolute molar concentration of melanin pigments by a simple pixelwise computation of the concentration according to $C = \overline{\Delta T}_{max}/m$. The concentration limit of detection for a 33-mW incident excitation laser power is determined by the 0.1-K temperature sensitivity of our thermal camera and by the temperature/concentration slope $m = 254 \text{ KM}^{-1}$ and equals $4 \cdot 10^{-4} \text{ M}$, corresponding to a 0.07 mg mL^{-1} concentration based on the eumelanin monomer molar mass 171 g mol^{-1} [44]. Such a concentration sensitivity could be further improved by incrementing the excitation laser power up to the maximum value allowed by the absence of photo-induced sample damage.

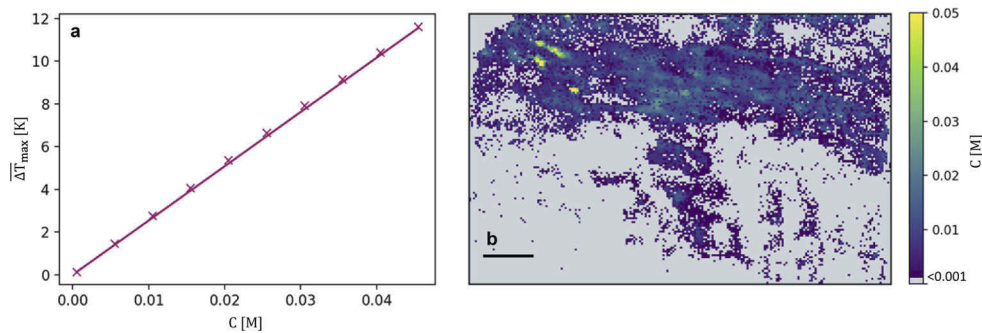


Fig. 2. Melanin molar concentration imaging. (a) $\overline{\Delta T}_{max}$ dependence on the absolute molar concentration C of light-absorbing and heat-releasing entities simulated based on Eq. (1) and (2) for a single-layer 1020- μm thick slab with $k = 0.9 \text{ W/(mK)}$, $D = 5.02 \cdot 10^{-7} \text{ m}^2/\text{s}$, $\omega = 30 \mu\text{m}$, $P_{\text{eff}} = 39.6 \text{ mW}$, $\tau_{\text{on}} = 200 \text{ ms}$ and $d = 420 \mu\text{m}$. The solid line is the best linear fit to $\overline{\Delta T}_{max} = mC$ with zero intercept and $m = 254 \text{ K/M}$. (b) Super-resolution image of the absolute molar concentration of melanin pigments in the B16 melanoma biopsy employed for Fig. 1(a). The image is derived from Fig. 1(a) by the pixel-wise conversion $C = \overline{\Delta T}_{max}/m$. Scale bar = 1000 μm .

The super-resolved thermal image of Fig. 1(a) is converted into a concentration image in Fig. 2(b). The retrieved melanin concentration up to 0.05 M (9 mg mL^{-1}) is comparable with reference values reported in the literature for human melanoma and human retinal pigment epithelium ex-vivo [28,45]. The reproducibility in the magnitude of the detected thermal signal (Fig. 1(f)) confirms the feasibility of a quantitative comparison of the melanin concentration maps extracted from different melanoma biopsies imaged under identical conditions.

We finally briefly discuss the uncertainty affecting recovered concentration values. In deriving the slope m of the $\overline{\Delta T}_{max}$ versus C plot based on Eq. (1) and (2), a fixed width has been assumed for the setup point-spread-function according to the prediction of Abbe's law for 10- μm thermal radiation. The effect of adopting a fixed (265 μm) Gaussian width can be quantified by deriving the slope m with varying PSF widths ranging from 220 μm to 300 μm . The computation of the first and second moments of the Planck's distribution in the spectral bandwidth of our thermal camera (7.5-13 μm) reveals indeed that the thermal radiation of samples at (and close to) room temperature peaks at 10- μm wavelength with 1.5- μm standard deviation: the two values 220- and 300- μm for the PSF width correspond therefore to the predictions of Abbe's law at the two

extreme 8.5- μm and 11.5- μm wavelength values. The slope m equals 271 KM^{-1} and 239 KM^{-1} for the 220- and the 300- μm PSF widths, respectively, with a maximum 6.7% deviation from the constant value 254 KM^{-1} adopted for Fig. 2(b). For each concentration value recovered as $C = \overline{\Delta T_{\max}}/m$, the uncertainty on the slope m propagates together with the 0.1-K uncertainty on the amplitude $\overline{\Delta T_{\max}}$ to define the overall uncertainty on C . For a typical 1-K temperature increment, we can estimate a $\sim 10\%$ relative uncertainty on the concentration. In deriving the necessary formalism via Eq. (1) and (2), we have further assumed light scattering by melanin pigments is negligible relatively to absorption and transmission at 514 nm. Such an approximation is justified for dilute well-solubilized melanin solutions [41], but might require refinements in the presence of particle aggregation and represents a second source of uncertainty in the estimate of the melanin concentration via the relation $C = \overline{\Delta T_{\max}}/m$.

2.3. Correlation between the photo-thermal signal amplitude and the size of the cell nuclei

The histograms of the amplitudes of laser-primed temperature increments (Fig. 1(f)) detected on murine melanoma biopsies (or equivalently, the corresponding histograms of the melanin concentration) reveal a multi-peaked distribution, suggesting that two major populations, differing in the melanin content, contribute to the collected thermal signal. A third cellular population can be identified as the one corresponding to all areas of the biopsy where no thermal signal exceeding the camera sensitivity has been detected. Aiming at further elucidating the presence of different cell populations in the imaged biopsies, a multimodal combination of super-resolved thermography and fluorescence confocal microscopy has been adopted. Following infrared thermography experiments, the same B16 murine melanoma biopsies have been fluorescently stained with the DRAQ5 dye, that specifically stains DNA with a broad fluorescence emission above 665 nm. The exemplary confocal fluorescence image reported in Fig. 3(a) highlights a pronounced heterogeneity in the dimensions of cellular nuclei. Quantitatively, an automated Watershed segmentation of individual nuclei (*methods* section) and the measurement of the corresponding occupied area (Fig. 3(d)-(e)) demonstrates significantly different nuclear sizes (Fig. 3(f)) in the two regions of interest of Fig. 3(b),(c). Extension of the segmentation procedure to the entire $\sim 2.5 \text{ mm}^2$ region of Fig. 3(a) provides a broad overall distribution for the nuclear size (Fig. 3(f)), with a two-component Gaussian fit identifying two distribution centers at $A_1 = (37 \pm 12) \mu\text{m}^2$ and $A_2 = (72 \pm 27) \mu\text{m}^2$.

Based on nuclei segmentation, a nuclear-size image can be reconstructed with the color code assigned by the average nuclear size retrieved in each pixel (*methods* section). If the same 37.8- μm pixel size of super-resolved photo-thermal images is adopted, the nuclear size map (Fig. 3(g)) can be correlated with the same region of interest of the corresponding thermal image (Fig. 3(h)). Indeed, the box-chart analysis of Fig. 3(i) reveals that those pixels where no thermal signal above the camera sensitivity has been detected (group A) appear to be associated to the largest average nuclear area $A_{\overline{\Delta T_{\max}} < 0.1\text{K}} = (70 \pm 35) \mu\text{m}^2$ (mean \pm standard deviation). If a 0.8-K temperature threshold is selected according to the separation of the two peaks in the $\overline{\Delta T_{\max}}$ histograms of Fig. 1(f), the pixel-wise comparison of Fig. 3(g) and Fig. 3(h) reveals that those pixels where the amplitude $\overline{\Delta T_{\max}}$ is comprised between the camera sensitivity and 0.8 K (group B) correspond to an average nuclear area $A_{0.1\text{K} \leq \overline{\Delta T_{\max}} < 0.8\text{K}} = (60 \pm 30) \mu\text{m}^2$, and that those pixels where the amplitude $\overline{\Delta T_{\max}}$ exceeds 0.8 K (group C) correspond to an average nuclear area $A_{\overline{\Delta T_{\max}} \geq 0.8\text{K}} = (50 \pm 30) \mu\text{m}^2$ (Fig. 3(i)).

The statistical significance of the difference between the mean nuclear area of group A and the mean nuclear area of both groups B and C (Fig. 3(i), $p < 0.001$) highlights an inverse correlation between the amplitude of laser-primed temperature increments and the cellular nucleus size, with the cells with the largest nuclei not providing any $> 0.1\text{-K}$ temperature increment. In this sense, provided that the photo-thermal effect is specifically ascribed to melanin pigments, the nuclear

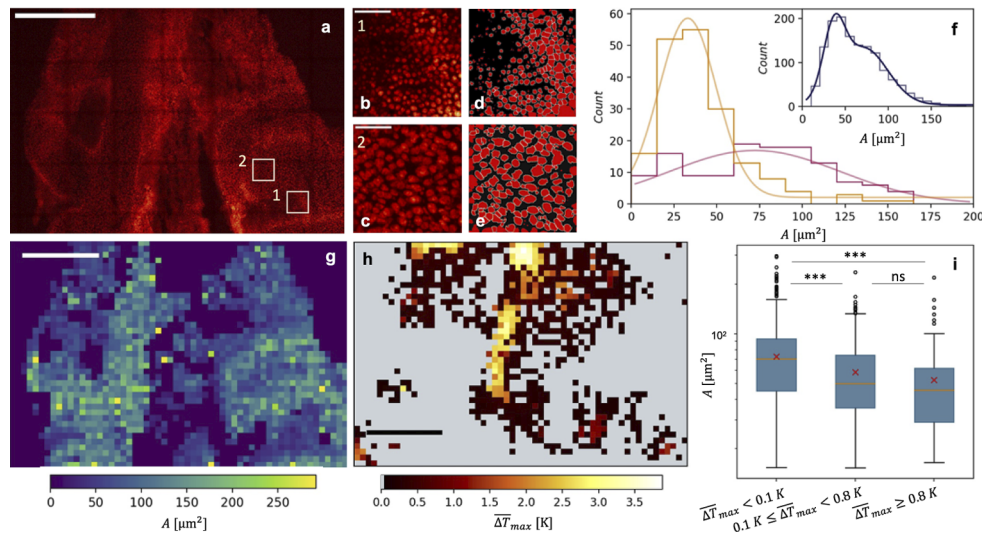


Fig. 3. Nuclei segmentation on a B16 melanoma biopsy. (a) Confocal fluorescence image ($\lambda_{\text{exc}} = 633$ nm, $\lambda_{\text{em}} = 660$ -700 nm) of a region of interest of a B16 murine melanoma biopsy (maximum z-projection over 9 planes sampled at 2.5- μm z-step). Cell nuclei are stained with the DRAQ5 dye. (b,c) Magnification of ROIs 1 and 2 from panel (a). (d,e) Results of the automated nuclei segmentation on panels (b,c), with borders of segmented nuclei highlighted in white. (f) Histograms of the areas of segmented nuclei from (d) and (e) (orange and pink, respectively). Best Gaussian fits provide average nuclear sizes (33 ± 17) μm^2 and (72 ± 50) μm^2 . Inset: histogram of the areas of segmented nuclei from panel (a), overlaid to the best two-component Gaussian fit centered at $A_1 = (37 \pm 12)$ μm^2 and $A_2 = (72 \pm 27)$ μm^2 . (g) Nuclear size map recovered from the nuclei segmentation on panel (a). Dark blue areas correspond to regions where nuclei are not sufficiently contrasted for the segmentation procedure. (h) Super-resolution thermal image acquired on the same biopsy (same region of panel (a)) prior to fluorescence staining. The 37.8- μm pixel size is the same for (g) and (h). Scale bars=500 μm in (a), (g), (h), 50 μm in (b)-(e). (i) Box chart of average nuclear sizes retrieved in pixels where a laser-primed temperature increment ΔT_{max} has been measured below 0.1 K (left, group A), above 0.8 K (right, group C) and within the 0.1-0.8 K range (middle, group B) (black circles = outliers, red cross = mean, orange line = median). Data have been tested for statistical significance with the Brown-Forsythe and Welch ANOVA test (***: $p < 0.001$, ns: $p > 0.12$).

size appears to discriminate melanin-containing cells from amelanotic cells. In the literature, the melanin concentration is pointed out as a marker for melanocyte differentiation [9] and is strictly related to the degree (stage I to IV) of maturation of melanosomes [46]. Recent experiments on B16-F10 ear-pinnae-implanted primary tumors have revealed an accumulation of melanosomes in poorly pigmented proliferating melanoma cells, suggesting that most of the melanosomes in the proliferative phase are amelanotic (i.e., in stage I-II) [38]. Proliferative activity has been pointed out in turn to be positively correlated to the mean nuclear area, with nuclei of proliferating cells exhibiting higher mean surface in melanocytic skin tumors [39]. This suggests that those cells not providing a detectable thermal signal and possessing a low melanin content below our $4 \cdot 10^{-4}$ M detection sensitivity correspond to the largest, and most likely highly proliferating, melanocytes.

The two populations contributing to a non-zero detected thermal signal appear unresolved instead in the overall nuclear-size distribution of Fig. 3(f) (the mean nuclear areas of groups B and C in Fig. 3(i) are not statistically different at the 0.05 level). Therefore, in this case the nuclear size is not directly correlated to the melanin content, and super-resolution photo-thermal imaging

is capable of differentiating two cellular populations with same-size nuclei but different melanin content. Based on the above discussion, the biological origin of the double temperature peak in Fig. 3(e),(f) is still unclear. Even if an analogous bimodal distribution has been reported for the length of melanosomes isolated from bovine retinal pigment epithelium [47], no similar evidence has been reported for murine melanosomes. Furthermore, considering the \sim micrometer size of melanosomes, we reason that the \sim 40- μ m resolution of our technique does not readily enable the discrimination of different melanosomal populations, and that such a discrimination is unlikely at the basis of the temperature peaks evidenced by super-resolved thermography. Future efforts will be devoted to further identify the two different cellular subtypes observed in the B16 tissue sections and to elucidate whether the double-peaked distribution of laser-primed temperature variations can be related to cellular features endowed with clinically relevant diagnostic power: on the basis of our results, we envision the possibility of exploiting a photo-thermal analysis to extract additional features to discriminate healthy and cancerous tissue and/or to stage the temporal evolution of melanomas.

3. Conclusion

Super-resolved photo-activated thermal imaging is proposed here as a powerful approach for the high-resolution spatial mapping of the absolute concentration of melanin pigments in excised melanoma biopsies. The technique takes advantage of a compact, low-cost benchtop microscope and relies on the accurate a-posteriori localization of laser-primed temperature variations to reconstruct the distribution of light-absorbing and heat-releasing entities in the sample with sub-diffraction \sim 40- μ m resolution. In particular, excitation at 514 nm allows exploiting the peculiar broadband absorption and thermal relaxation properties of melanin to image pigments in label-free configuration. Melanin specificity is ensured by the fact that melanin is the dominant photo-thermal chromophore in pigmented skin lesions [48], with 0.99 thermal relaxation efficiency [42] and an absorption coefficient about four times higher than the absorption coefficient of hemoglobin at 514 nm [29,49]. Label-free imaging allows avoiding the Fontana-Masson (FM) technique [50] as well as lengthy formalin-fixed paraffin-embedded (FFPE) immunohistochemical melanoma-black-45, Melan-A or S-100 exogenous stains [21]. The FM method, which has turned into the gold standard to identify melanin granules in FFPE and frozen tissues, is based on the visualization of the insoluble black precipitate that results from the reduction of ammoniacal silver to metallic silver due to the presence of melanin in melanosomes [50]. Super-resolved thermography provides the spatial distribution of melanin pigments with lower spatial resolution relatively to the FM method (and to its more recent and sophisticated implementations, such as the FMPS method [50]), but it outperforms the FM stain in enabling the quantification of the absolute melanin concentration. The space-resolved quantification of melanin represents the main advantage of sub-diffraction thermal imaging in comparison to standard melanin stains.

By the numerical integration of the full 3D heat transfer model, we have indeed proposed and demonstrated the data-analysis protocol to convert temperature-based maps into quantitative images of the melanin absolute molar concentration. Our $4 \cdot 10^{-4}$ M lower limit of detection defined by the adopted 33-mW excitation power and by the thermal-camera temperature sensitivity has proven sufficient to investigate melanin in the \sim 0.1-10 mg mL⁻¹ concentration range, which is comparable to what is reported for both human melanoma and human retinal pigment epithelium in the literature [28,45].

By combining the implementation of super-resolution image acquisition (which retains fundamental importance to enable the characterization of pigmented skin lesions on the tissue spatial scale) with the quantification of the melanin absolute concentration, the proposed approach significantly expands the applicability of infrared thermography in the context of melanoma screening and diagnosis. In fact, even though dermatology is a compelling application area for infrared thermal imaging [51], to date conventional thermography has been limited to a

few pioneering and debated qualitative clinical studies [52], aimed for example at the in-vivo malignancy-benignancy discrimination of pigmented lesions [51] or at the patient follow-up after treatment [53] based on spatially-averaged temperature measurements. For the first time, our results extend far-infrared thermography to the space-resolved melanin-based imaging of mm²- to cm²-sized explanted biopsies: provided the crucial role played by melanin pigments in regulating the overall melanoma development and evolution, our strategy could represent a useful complement to more traditional histopathological analyses of explanted skin sections. Demonstrated here on murine B16 melanoma, the very same technique could be readily extended without necessary adaptation to the inspection of ex-vivo human melanoma biopsies in the clinical setting. With approximately 90% of all human invasive melanomas being classified as melanocytic [48], we envision broad applicability for melanin-based photo-thermal imaging of excised biopsies.

We finally remark that super-resolution thermography operates here in reflection mode (the thermal radiation is collected from the sample front surface), and could in principle be extended to the analysis of bulk tissue samples: the extraction of light-induced temperature depth profiles in thick specimens would represent a significant extension of the super-resolution imaging method presented here [54]. In the context of melanoma screening, the reconstruction of a tomographic image of light absorbing entities in the sample would be extremely useful when performed in-vivo, where the assessment of the melanoma thickness has been established as an important histologic predictor of the patient outcome [55]. At least two major modifications would however be required for the in-vivo extension of our approach. First, the data analysis protocol should be modified to account for the multiple photo-thermal populations of melanin and oxy- and deoxy- hemoglobin: the blood content and the contribution of blood chromophores are expected to be significantly lower in excised biopsies than in vascularized tissues in-vivo [48], where they should instead be accounted for with a properly modified theoretical treatment. Second, the total imaging time should be suitably shortened. In the current implementation of super-resolution thermal imaging, a region 4.5×2.3 mm² in size can be scanned in 60 minutes. Such a data-acquisition time could be reduced by multi-spot laser excitation and by relaxing the constraints on the observation of isolated temperature peaks. Near-future efforts will be devoted to the possibility of accommodating the fit of multiple overlapping temperature peaks in the raw thermal camera frames.

4. Methods

4.1. Super-resolution photo-thermal imaging

Super-resolution thermal imaging is performed on a custom-made benchtop optical setup [35] as depicted in Fig. S7. Absorption in the sample is primed by an Argon laser beam (514-nm wavelength, Spectra Physics, CA, USA) with $1/e^2$ spot diameter $\omega = 30$ μ m and typical 30-mW power on the sample plane. A scanning unit with servo-board electronics and two galvanometric mirrors (MicroMax Series 670, Cambridge Technology Inc., MA, USA) is combined to a two-lens scan system (4- and 10-cm focal lengths), followed by beam focalization (10-cm lens focal length) onto the sample plane. The mirror positioning system is driven by a programmable National Instrument board (LabVIEW RIO, National Instruments, TX, USA) to operate the mirrors in a conventional raster-scanning mode (40- μ m typical pixel size on the sample plane); user-defined voltage values are supplied to the mirrors to regulate the scan path length along the horizontal and vertical axes.

The same board driving the scan system is also employed to synchronize the galvanometric mirrors with a programmable electronic shutter (Oriel 76992, Newport, CA, USA; 150 Hz maximum operation frequency) aimed at modulating the laser illumination in time. By selectively activating the laser illumination on the sample plane during the laser raster scanning [35] a minimum distance is ensured between consecutively induced temperature increments, thereby

allowing the detection of one isolated temperature peak at a time [35]. During laser de-activation (i.e., shutter closure), a default 6-ms pixel dwell time of the laser beam along the scan grid is usually adopted. During laser activation, the shutter opening time is set to the desired value $\tau_{\text{on}} = 200$ ms and the laser pixel dwell time is temporarily increased to the same value. We report the details of the laser scan path in Fig. S7.

The detection of thermal radiation is performed in the 7.5-13- μm spectral range by an uncooled microbolometer-based thermal camera (FLIR T650sc, FLIR Systems Inc., OR, USA) with 30-Hz frame rate. The detector provides 640×480 images, with 420- μm pixel size on the sample plane, and signal detection is performed in reflection mode (i.e., thermal radiation is collected from the sample front surface as depicted in Fig. S7). The thermo-camera corrects for the atmospheric attenuation and the sample reflection of the thermal radiation emitted by the surroundings provided that the sample distance from the camera front lens, the sample emissivity ε , and the relative humidity and temperature of the atmosphere are inserted in the camera software. A 50% humidity has been assumed for all the experiments of the present work, whereas the sample distance (~ 40 cm) and the ambient temperature have been measured for each imaging experiment. An emissivity $\varepsilon = 0.98$ has been employed as reported for skin in the literature [56]. The analysis of raw thermal camera frames has been performed by the two-dimensional non-linear Gaussian fit of each detected temperature peak at the end of the corresponding laser illumination event lasting τ_{on} ; each fit provides the peak center coordinates and the amplitude $\overline{\Delta T}_{\text{max}}$ [35].

4.2. Transmission and fluorescence microscopy setup

A Leica TCS SP5 STED-CW scanning confocal microscope (Leica Microsystems, D) has been employed for transmitted-light and fluorescence imaging of melanoma biopsies. The laser source consists in a 633-nm He-Ne beam or a 514-nm Argon beam (power $P \sim 10$ μW on the sample plane), which is focused on the sample by a 20x 0.5-N.A. air objective (HCX PL Fluotar, Leica Microsystems, D). Transmitted-light images have been acquired on both stained and unstained melanoma biopsies by detecting the transmitted laser light signal with a non-spectral dedicated photo-multiplier tube, with no confocal pinhole along the detection optical path. For DRAQ5 stained biopsies, the dye fluorescence signal has been collected by a PMT (Photo-Multiplier Tube) in the 660-700 nm band. A 400-Hz raster scan frequency per line has been adopted, and millimeter-sized sample regions have been imaged using a tile-scan (mosaic) acquisition mode.

4.3. B16 biopsies

For the preparation of murine B16 melanoma biopsies, the murine tumor cell line B16 has been cultured in IMDM-10 complete medium (IMDM, 10% heat-inactivated FBS (EuroClone, I), 2 mM l-glutamine, 100 U/ml penicillin, 100 $\mu\text{g}/\text{ml}$ streptomycin). Cells at 70% confluence have been collected for injection of a tumorigenic dose of $2 \cdot 10^6$ cells in the deep derma of the left flank of C57bl/6 mice at 7-12 weeks of age. At day 7 or day 14, mice have been euthanized and the tumor has been collected. Explanted tissue sections have been cut on a cryostat in 20- μm sections upon embedding in OCT freezing medium (Biooptica, I) and adhered to glass slides (Superfrost Plus, Thermo Fisher Scientific, MA, USA) for super-resolution photo-thermal imaging. When necessary, fluorescence staining with the DRAQ5 nucleic-acid stain has been performed after completion of photo-thermal data acquisition on the biopsies. For hematoxylin-and-eosin staining the skin sections have been stained with Meyer's hematoxylin solution for 8 minutes and then washed in warm running tap water for 5 minutes. Sections have been stained with Eosin Y solution for 1 minute, washed in warm running water for 5 minutes, rinsed in distilled water and then dehydrated through passages in 95% and absolute alcohol. Slides have been cleared in xylene and mounted with Eukitt. Images have been acquired with a NanoZoomer scanner (Hamamatsu, JP).

All the experiments have been performed under protocols approved by the Institutional Animal Care and Use Committee of the University of Milano-Bicocca and the Italian Ministry of Health.

4.4. Nuclei segmentation

The automatic segmentation of cellular nuclei from fluorescence confocal microscopy images has been implemented in a custom-written macro in the freeware software FiJi [57]. The macro reads the raw fluorescence image in .tif format and routinely performs the nuclei segmentation on adjacent Regions of Interest (ROI) of adjustable size (typically, 3000×3000 pixels with ~ 250 -nm pixel size). For each ROI, a Gaussian blur filter with 1.5-pixel standard deviation is applied first; then the ROI image gets converted into a binary file upon selection of an intensity threshold and separation of individual nuclei by the FiJi built-in Watershed algorithm. The nuclei segmentation is performed based on the FiJi “Analyze particle” tool with acceptable identified nucleus radius in the $15\text{--}300\ \mu\text{m}^2$ range, with acceptable nucleus circularity in the 0.2–1 range, and by excluding all nuclei located on the ROIs edge. Results of the segmentation procedure are saved in a .txt file as a list of the area and center coordinates of each nucleus, so that a final image with chosen pixel size can be reconstructed and color-coded based on the average area of all the nuclei identified in each pixel.

4.5. Data analysis software

Photo-thermal imaging raw data have been acquired with the thermo-camera software (FLIR Tools+, FLIR Systems Inc., OR, USA), exported in .csv file format and entirely processed by a custom-written Python code. A custom Python code has also been employed for the numerical integration of Eq. (1) and Eq. (2) for Fig. 2. Finite-element simulations employed for Fig. S5 and Fig. S6 have been performed by the COMSOL Multiphysics software (COMSOL AB, S). Statistical significance tests in Fig. 3 have been performed by GraphPad Prism (GraphPad Software, CA, USA).

Funding. Horizon 2020 Framework Programme (964481); Università degli Studi di Milano-Bicocca (2018-ATE-0070, 2019-ATE-0126).

Acknowledgments. The authors acknowledge funding from the European Union’s Horizon 2020 research and innovation programme under grant agreement No. 964481 (FET Open project “IN2SIGHT”). The authors also acknowledge funding (2018-ATE-0070 and 2019-ATE-0126) from Università degli Studi di Milano-Bicocca.

Disclosures. The authors declare no conflicts of interest.

Data availability. Data underlying the results presented in this paper may be obtained from the authors upon reasonable request.

Supplemental document. See [Supplement 1](#) for supporting content.

References

1. A. H. Shain and B. C. Bastian, “From melanocytes to melanomas,” *Nat. Rev. Cancer* **16**(6), 345–358 (2016).
2. M. Sarna, M. Krzykawska-Serda, M. Jakubowska, A. Zadło, and K. Urbanska, “Melanin presence inhibits melanoma cell spread in mice in a unique mechanical fashion,” *Sci. Rep.* **9**(1), 9280 (2019).
3. J. Y. Lin and D. E. Fisher, “Melanocyte biology and skin pigmentation,” *Nature* **445**(7130), 843–850 (2007).
4. J. X. Wang, M. Fukunaga-Kalabis, and M. Herlyn, “Crosstalk in skin: melanocytes, keratinocytes, stem cells, and melanoma,” *J. Cell Commun. Signal.* **10**(3), 191–196 (2016).
5. H. Sung, J. Ferlay, R. L. Siegel, M. Laversanne, I. Soerjomataram, A. Jemal, and F. Bray, “Global Cancer Statistics 2020: GLOBOCAN estimates of incidence and mortality worldwide for 36 cancers in 185 countries,” *CA A Cancer J Clin* **71**(3), 209–249 (2021).
6. F. Kuzu, F. D. Nguyen, M. A. Noory, and A. Sharma, “Current state of animal (mouse) modeling in melanoma research,” *Cancer Growth Metastasis* **8**(s1), 81–94 (2015).
7. A.-M. Forsea, “Melanoma epidemiology and early detection in europe: diversity and disparities,” *Dermatol Pract Concept* **10**(3), e2020033 (2020).
8. J. K. C. Chan, “The wonderful colors of the hematoxylin-eosin stain in diagnostic surgical pathology,” *Int J Surg Pathol* **22**(1), 12–32 (2014).

9. T. E. Matthews, I. R. Piletic, M. A. Selim, M. J. Simpson, and W. S. Warren, "Pump-probe imaging differentiates melanoma from melanocytic nevi," *Sci. Transl. Med.* **3**(71), 71ra15 (2011).
10. S. Guo, S. Pfeifenbring, T. Meyer, G. Ernst, F. von Eggeling, V. Maio, D. Massi, R. Cicchi, F. S. Pavone, J. Popp, and T. Bocklitz, "Multimodal image analysis in tissue diagnostics for skin melanoma," *J. Chemom.* **32**(1), 1–17 (2018).
11. R. Scodellaro, M. Bouzin, F. Mingozzi, L. D'Alfonso, F. Granucci, M. Collini, G. Chirico, and L. Sironi, "Whole-section tumor micro-architecture analysis by a two-dimensional phasor-based approach applied to polarization-dependent second harmonic imaging," *Front. Oncol.* **9**(JUN), 1–14 (2019).
12. R. M. Slominski, M. A. Zmijewski, and A. T. Slominski, "The role of melanin pigment in melanoma," *Exp. Dermatol.* **24**(4), 258–259 (2015).
13. C. Grieco, F. R. Kohl, A. T. Hanes, and B. Kohler, "Probing the heterogeneous structure of eumelanin using ultrafast vibrational fingerprinting," *Nat. Commun.* **11**(1), 4569 (2020).
14. D. Fu, T. Ye, T. E. Matthews, G. Yurtsever, and W. S. Warren, "Two-color, two-photon, and excited-state absorption microscopy," *J. Biomed. Opt.* **12**(5), 054004 (2007).
15. A. A. Brozyna, W. Józwicki, J. A. Carlson, and A. T. Slominski, "Melanogenesis affects overall and disease-free survival in patients with stage III and IV melanoma," *Hum. Pathol.* **44**(10), 2071–2074 (2013).
16. A. A. Brozyna, W. Józwicki, K. Roszkowski, J. Filipiak, and A. T. Slominski, "Melanin content in melanoma metastases affects the outcome of radiotherapy," *Oncotarget* **7**(14), 17844–17853 (2016).
17. A. Slominski, T. K. Kim, A. A. Brozyna, Z. Janjetovic, D. L. P. Brooks, L. P. Schwab, C. Skobowiat, W. Józwicki, and T. N. Seagroves, "The role of melanogenesis in regulation of melanoma behavior: melanogenesis leads to stimulation of HIF-1 α expression and HIF-dependent attendant pathways," *Arch. Biochem. Biophys.* **563**, 79–93 (2014).
18. S. Chung, G. J. Lim, and J. Y. Lee, "Quantitative analysis of melanin content in a three-dimensional melanoma cell culture," *Sci. Rep.* **9**(1), 1–9 (2019).
19. B. Fernandes, T. Matamá, D. Guimarães, A. Gomes, and A. Cavaco-Paulo, "Fluorescent quantification of melanin," *Pigment Cell Melanoma Res.* **29**(6), 707–712 (2016).
20. S. Ito and K. Jimbow, "Quantitative analysis of eumelanin and pheomelanin in hair and melanomas," *J. Invest. Dermatol.* **80**(4), 268–272 (1983).
21. C.-K. Sun, P.-J. Wu, S.-T. Chen, Y.-H. Su, M.-L. Wei, C.-Y. Wang, H.-C. Gao, K.-B. Sung, and Y.-H. Liao, "Slide-free clinical imaging of melanin with absolute quantities using label-free third-harmonic-generation enhancement-ratio microscopy," *Biomed. Opt. Express* **11**(6), 3009 (2020).
22. Z. Huang, H. Lui, X. K. Chen, A. Alajlan, D. I. McLean, and H. Zeng, "Raman spectroscopy of in vivo cutaneous melanin," *J. Biomed. Opt.* **9**(6), 1198 (2004).
23. Q. Godechal, G. E. Ghanem, M. G. Cook, and B. Gallez, "Electron paramagnetic resonance spectrometry and imaging in melanomas: comparison between pigmented and nonpigmented human malignant melanomas," *Mol. Imaging* **12**(4), 218–223 (2013).
24. E. Dimitrow, I. Riemann, A. Ehlers, M. J. Koehler, J. Norgauer, P. Elsner, K. König, and M. Kaatz, "Spectral fluorescence lifetime detection and selective melanin imaging by multiphoton laser tomography for melanoma diagnosis," *Exp. Dermatol.* **18**(6), 509–515 (2009).
25. S. Guida, F. Arginelli, F. Farnetani, S. Ciardo, L. Bertoni, M. Manfredini, N. Zerbinati, C. Longo, and G. Pellacani, "Clinical applications of in vivo and ex vivo confocal microscopy," *Appl. Sci.* **11**(5), 1979 (2021).
26. J. Malvehy, J. Pérez-Anker, A. Toll, R. Pigem, A. García, L. L. Alos, and S. Puig, "Ex vivo confocal microscopy: revolution in fast pathology in dermatology," *Br. J. Dermatol.* **183**(6), 1011–1025 (2020).
27. D. Fu, T. Ye, T. E. Matthews, J. Grichnik, L. Hong, J. D. Simon, and W. S. Warren, "Probing skin pigmentation changes with transient absorption imaging of eumelanin and pheomelanin," *J. Biomed. Opt.* **13**(5), 054036 (2008).
28. X. Shu, H. Li, B. Dong, C. Sun, and H. F. Zhang, "Quantifying melanin concentration in retinal pigment epithelium using broadband photoacoustic microscopy," *Biomed. Opt. Express* **8**(6), 2851 (2017).
29. J. He, N. Wang, H. Tsurui, M. Kato, M. Iida, and T. Kobayashi, "Noninvasive, label-free, three-dimensional imaging of melanoma with confocal photothermal microscopy: differentiate malignant melanoma from benign tumor tissue," *Sci. Rep.* **6**(1), 30209 (2016).
30. T. Kobayashi, K. Nakata, I. Yajima, M. Kato, and H. Tsurui, "Label-free imaging of melanoma with confocal photothermal microscopy: differentiation between malignant and benign tissue," *Bioengineering* **5**(3), 67 (2018).
31. J. He, J. Miyazaki, N. Wang, and T. Kobayashi, "Label-free imaging of melanoma with nonlinear photothermal microscopy," *Opt. Lett.* **40**(7), 1141–1144 (2015).
32. J. Miyazaki and T. Kobayashi, "Photothermal microscopy for high sensitivity and high resolution absorption contrast imaging of biological tissues," *Photonics* **4**(2), 32 (2017).
33. X. Han, H. Lui, D. I. McLean, and H. Zeng, "Near-infrared autofluorescence imaging of cutaneous melanins and human skin in vivo," *J. Biomed. Opt.* **14**(2), 024017 (2009).
34. S. Kalia, J. Zhao, H. Zeng, D. McLean, N. Kollias, and H. Lui, "Melanin quantification by in vitro and in vivo analysis of near-infrared fluorescence," *Pigment Cell Melanoma Res.* **31**(1), 31–38 (2018).
35. M. Bouzin, M. Marini, A. Zeynali, M. Borzenkov, L. Sironi, L. D'Alfonso, F. Mingozzi, F. Granucci, P. Pallavicini, G. Chirico, and M. Collini, "Photo-activated raster scanning thermal imaging at sub-diffraction resolution," *Nat. Commun.* **10**(1), 5523 (2019).

36. M. Marini, M. Bouzin, L. Sironi, L. D'Alfonso, R. Colombo, D. Di Martino, G. Gorini, M. Collini, and G. Chirico, "A novel method for spatially-resolved thermal conductivity measurement by super-resolution photo-activated infrared imaging," *Mater. Today Phys.* **18**, 100375 (2021).
37. M. Vollmer and K. P. Möllmann, *Infrared Thermal Imaging: Fundamentals, Research and Applications* (Wiley-Vch, 2017).
38. M. Potez, V. Trappetti, A. Bouchet, C. Fernandez-Palomo, E. Güç, W. W. Kilarski, R. Hlushchuk, J. Laissue, and V. Djonov, "Characterization of a B16-F10 melanoma model locally implanted into the ear pinnae of C57BL/6 mice," *PLoS One* **13**(11), e0206693 (2018).
39. J. Smolle, R. Hofmann-Wellenhof, H. P. Soyer, H. Stettner, and H. Kerl, "Nuclear size and shape parameters correlate with proliferative activity in cutaneous melanocytic tumors," *J. Invest. Dermatol.* **93**(1), 178–182 (1989).
40. D. Bäuerle, *Laser Processing and Chemistry* (Springer Berlin Heidelberg, 2011).
41. J. Riesz, J. Gilmore, and P. Meredith, "Quantitative scattering of melanin solutions," *Biophys. J.* **90**(11), 4137–4144 (2006).
42. P. Meredith and J. Riesz, "Radiative relaxation quantum yields for synthetic eumelanin," *Photochem. Photobiol.* **79**(2), 211 (2004).
43. M. A. Ansari and E. Mohajerani, "Mechanisms of laser-tissue interaction: I. optical properties of tissue," *J. Lasers Med. Sci.* **2**(3), 119–125 (2011).
44. I. R. Piletic, T. E. Matthews, and W. S. Warren, "Estimation of molar absorptivities and pigment sizes for eumelanin and pheomelanin using femtosecond transient absorption spectroscopy," *J. Chem. Phys.* **131**(18), 181106 (2009).
45. T. Morishima and E. Fukuda, "Quantitative analysis of eumelanin and pheomelanin in human malignant-melanoma tissues," *Arch. Dermatol. Res.* **277**(3), 248–250 (1985).
46. M. Fukuda, "Lysosome-related organelles," *Encycl. Cell Biol.* **2**, 235–242 (2016).
47. Y. Liu, L. Hong, K. Wakamatsu, S. Ito, B. B. Adhyaru, C.-Y. Cheng, C. R. Bowers, and J. D. Simon, "Comparisons of the structural and chemical properties of melanosomes isolated from retinal pigment epithelium, iris and choroid of newborn and mature bovine eyes," *Photochem. Photobiol.* **81**(3), 510 (2005).
48. J. Hult, A. Merdasa, A. Pekar-Lukacs, M. Tordengren Stridh, A. Khodaverdi, J. Albinsson, B. Gesslein, U. Dahlstrand, L. Engqvist, Y. Hamid, D. Larsson Albér, B. Persson, T. Erlöv, R. Sheikh, M. Cinthio, and M. Malmjö, "Comparison of photoacoustic imaging and histopathological examination in determining the dimensions of 52 human melanomas and nevi ex vivo," *Biomed. Opt. Express* **12**(7), 4097 (2021).
49. I. V. Meglinski and S. J. Matcher, "Quantitative assessment of skin layers absorption and skin reflectance spectra simulation in the visible and near-infrared spectral regions," *Physiol. Meas.* **23**(4), 741–753 (2002).
50. V. S. Carriel, J. Aneiros-Fernandez, S. Arias-Santiago, I. J. Garzón, M. Alaminos, and A. Campos, "A novel histochemical method for a simultaneous staining of melanin and collagen fibers," *J. Histochem. Cytochem.* **59**(3), 270–277 (2011).
51. C. Herman, "The role of dynamic infrared imaging in melanoma diagnosis," *Expert Review of Dermatology* **8**(2), 177–184 (2013).
52. E. F. J. Ring and K. Ammer, "Infrared thermal imaging in medicine," *Physiol. Meas.* **33**(3), R33–R46 (2012).
53. G. A. Santa Cruz, J. Bertotti, J. Marín, S. J. González, S. Gossio, D. Alvarez, B. M. C. Roth, P. Menéndez, M. D. Pereira, M. Alberio, L. Cubau, P. Orellano, and S. J. Liberman, "Dynamic infrared imaging of cutaneous melanoma and normal skin in patients treated with BNCT," *Appl. Radiat. Isot.* **67**(7–8), S54–S58 (2009).
54. S. A. Telenkov, B. S. Tanenbaum, D. M. Goodman, J. S. Nelson, and T. E. Milner, "In vivo infrared tomographic imaging of laser-heated blood vessels," *IEEE J. Sel. Top. Quantum Electron.* **5**(4), 1193–1199 (1999).
55. L. Taylor, K. Hood, L. Reisch, J. Elmore, M. Piepkorn, R. Barnhill, S. Knezevich, A. Radick, and D. Elder, "Influence of variability in assessment of Breslow thickness, mitotic rate and ulceration among US pathologists interpreting invasive melanoma, for the purpose of AJCC staging," *J Cutan Pathol* **45**(8), 588–596 (2018).
56. V. Bernard, E. Staffa, V. Mornstein, and A. Bourek, "Infrared camera assessment of skin surface temperature - effect of emissivity," *Phys. Medica* **29**(6), 583–591 (2013).
57. J. Schindelin, I. Arganda-Carreras, E. Frise, V. Kaynig, M. Longair, T. Pietzsch, S. Preibisch, C. Rueden, S. Saalfeld, B. Schmid, J. Y. Tinevez, D. J. White, V. Hartenstein, K. Eliceiri, P. Tomancak, and A. Cardona, "Fiji: An open-source platform for biological-image analysis," *Nat. Methods* **9**(7), 676–682 (2012).